# Drop Shapes, Model Comparisons, and Calculations of Polarimetric Radar Parameters in Rain

M. Thurai, G. J. Huang, and V. N. Bringi

*Colorado State University, Fort Collins, Colorado*

W. L. Randeu

*Graz University of Technology, Graz, Austria*

M. Schönhuber

*Joanneum Research, Graz, Austria*

## ABSTRACT

Drop shapes derived from a previously conducted artificial rain experiment using a two-dimensional video disdrometer (2DVD) are presented. The experiment involved drops falling over a distance of 80 m to achieve their terminal velocities as well as steady-state oscillations. The previous study analyzed the measured axis ratios (i.e., ratio of maximum vertical to maximum horizontal chord) as a function of equivolumetric spherical drop diameter ($D_{eq}$) for over 115 000 drops ranging from 1.5 to 9 mm. In this paper, the actual contoured shapes of the drops are reported, taking into account the finite quantization limits of the instrument. The shapes were derived from the fast line-scanning cameras of the 2DVD. The drops were categorized into $D_{eq}$ intervals of 0.25-mm width and the smoothed contours for each drop category were superimposed on each other to obtain their most probable shapes and their variations due to drop oscillations. The most probable shapes show deviation from oblate spheroids for $D_{eq} > 4$ mm, the larger drops having a more flattened base, in good agreement with the equilibrium (nonoblate) shape model of Beard and Chuang. Deviations were noted from the Beard and Chuang model shapes for diameters larger than 6 mm. However, the 2DVD measurements of the most probable contour shapes are the first to validate the Beard and Chuang model shapes for large drops, and further to demonstrate the differences from the equivalent oblate shapes. The purpose of this paper is to document the differences in radar polarization parameters and the range of error incurred when using the equivalent oblate shapes versus the most probable contoured shapes measured with the 2DVD especially for drop size distributions (DSDs) with large median volume diameters ($>2$ mm).

The measured contours for $D_{eq} > 1.5$ mm were fitted to a modified conical equation, and scattering calculations were performed to derive the complex scattering amplitudes for forward and backscatter for H and V polarizations primarily at 5.34 GHz (C band) but also at 3 GHz (S band) and 9 GHz (X band). Calculations were also made to derive the relevant dual-polarization radar parameters for measured as well as model-based drop size distributions. When comparing calculations using the contoured shapes against the equivalent oblate spheroid shapes, good agreement was obtained for cases with median volume diameter ($D_0$) less than around 2 mm. Small systematic differences in the differential reflectivity ($Z_{dr}$) values of up to 0.3 dB were seen for the larger $D_0$ values when using the oblate shapes, which can be primarily attributed to the shape differences in the resonance region, which occurs in the 5.5–7-mm-diameter range at C band. Lesser systematic differences were present in the resonance region at X band (3–4 mm). At S band, the impact of shape differences in the polarimetric parameters were relatively minor for $D_0$ up to 2.5 mm. Unusual DSDs with very large $D_0$ values ($>3$ mm) (e.g., as can occur along the leading edge of severe convective storms or aloft due localized "big drop" zones) can accentuate the $Z_{dr}$ difference between the contoured shape and the oblate spheroid equivalent, especially at C band. For attenuation-correction schemes based on differential propagation phase, it appears that the equivalent oblate shape approximation is sufficient using a fit to the axis ratios from the 80-m fall experiment given in this paper. For high accuracy in developing algorithms for predicting $D_0$ from $Z_{dr}$, it is recommended that the fit to the most probable contoured shapes as given in this paper be used especially at C band.

---

*Corresponding author address:* Merhala Thurai, Dept. of ECE, Colorado State University, Fort Collins, CO 80523-1373.
E-mail: merhala@engr.colostate.edu

## 1. Introduction

Drop shapes in rain play a central role in the development of rain retrieval algorithms used for polarization weather radars (e.g., Bringi and Chandrasekar 2001, chapter 7). The majority of past studies have approximated the drop shapes to oblate spheroids, even though it is well known that larger drops tend to deviate from such an approximation (Pruppacher and Pitter 1971; Beard and Chuang 1987). Typically, the drop shape is simply characterized by an axis ratio, defined by the ratio between the maximum vertical and horizontal chords. An oblate spheroid model with the same axis ratio is then used in place of the "true" shape for applications involving dual polarization radar parameters, such as differential reflectivity ($Z_{dr}$) and specific differential propagation phase ($K_{dp}$).

At low-attenuating frequencies such as S band, drop shapes are used in the estimation of raindrop size distribution (DSD) and hence the rainfall rate from polarimetric radar measurements. At increasingly attenuating frequencies such as C band and above, the rainfall estimation method requires an added process of correcting for rain attenuation of the radar signal. Correction schemes that utilize $K_{dp}$ assume an equivalent oblate model to determine the copolar attenuation and the differential attenuation. Generally speaking, at higher frequencies, the attenuation-correction algorithms and the subsequent DSD retrievals are more sensitive to errors due to non-Rayleigh effects.

The shape information is also relevant in evaluating propagation effects on line-of-sight systems and earth–space communication links operating at microwave frequencies (Oguchi 1983; Olsen 1981; Allnutt 1989, chapters 4 and 5). Effects such as differential attenuation and rain-induced cross polarization, which are particularly relevant for systems employing orthogonal polarizations, are governed by the probable drop shapes and size distributions.

An earlier study (Thurai and Bringi 2005) reported on axis ratios measured using a two-dimensional video disdrometer (2DVD; Randeu et al. 2002; Kruger and Krajewski 2002) from an artificial rain experiment for drop diameters ranging up to 9 mm. The axis ratios were derived from the height to length ratios of the drop images. In this article, we present the actual contoured shapes of drops from that same experiment after accounting for the finite quantization limits of the instrument. The shapes were derived directly from the digitized data provided by fast line-scanning cameras of the 2DVD. Drop shape comparisons are made with the full (nonoblate) numerical model of Beard and Chuang (1987). The effects of approximating the shapes to ob-late spheroids are considered in terms of computations of dual-polarization radar parameters, primarily at C band but also at X and S bands.

## 2. Drop shapes from the 80-m fall experiment

### a. Previous results

The 80-m fall experiment (described in Thurai and Bringi 2005) involved drops being generated from a hose located on a bridge 80 m above ground, this height being the largest so far and assumed to be sufficient to allow drop oscillations to reach steady state. A 2DVD was located on the ground in order to capture images of the falling drops, under very light wind conditions. The total number of drops analyzed was around 115 000. Their axis ratio (ratio of maximum vertical to maximum horizontal chord) distributions were obtained for diameters ranging from 1.5 to 9 mm. Distributions of axis ratios for all diameters larger than 1.5 mm showed that they could be fitted to Gaussian distributions. Their fitted mean values were compared with past literature results and were shown to be in close agreement with those reported by Goddard et al. (1995) as well as the fitted equation given in Brandes et al. (2002). In addition, the axis ratio at the lower diameter end of the 2DVD data resolution (near 1.5 mm) were shown to merge closely with laboratory measurements of smaller drops at the 1.5-mm-diameter region (Beard and Kubesh 1991).

The images captured during this experiment by the 2DVD's fast scanning cameras were reprocessed using a contour smoothing procedure to construct the actual shape of each individual drop. Full details of the contour smoothing algorithms for the 2DVD data as well as their implementation can be found in Gimpl (2003). The appendix describes the methodology used herein.

### b. Probability contours

Each drop, after undergoing contour smoothing, was categorized into various equivolumetric sphere diameter intervals, ranging from 1.5 to 8 mm in 0.25-mm steps. Below 1.5 mm, the resolution of the 2DVD was not considered sufficient for accurate shape estimation. For each of the assigned diameter intervals, all drop contours in that category were superimposed exactly on each other to derive the probability contours, the probability values being normalized to the total number of pixels in all the drop contours in that diameter interval. In essence the contours represent a two-dimensional histogram of the $(x, y)$ coordinates obtained from the 2DVD data (see also the appendix), depicted in color scale as opposed to a 3D surface plot. It follows that
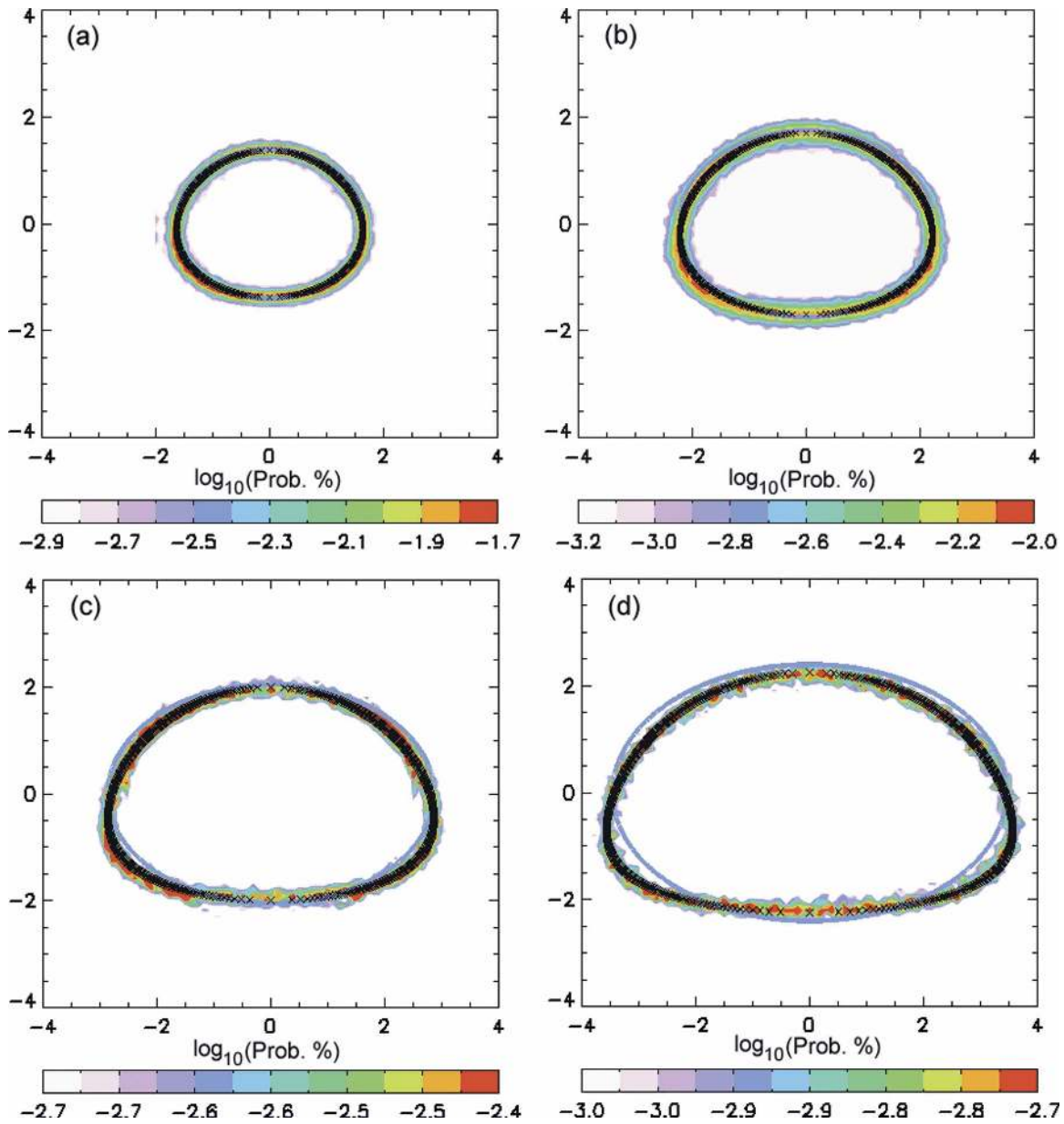
FIG. 1. Drop shapes given in terms of probability contours on a log scale indicated in color for (a) 3–3.25, (b) 4–4.25, (c) 5–5.25, and (d) 6–6.25 mm, the probability values being normalized with respect to the total number of pixels for all the drop contours in that diameter interval. Superimposed in black is the curve given by the fitted Eq. (1) obtained by modifying the shapes given in Wang (1982). Light blue curve shows the approximated oblate spheroid shapes whose axis ratios are from Thurai and Bringi (2005).

outliers will be diminished in their significance and the most probable $(x, y)$ coordinates will be highlighted. Figure 1 shows color images of these probability contours (in log scale) for equivalent drop diameters in the range (a) 3–3.25, (b) 4–4.25, (c) 5–5.25, and (d) 6–6.25 mm. The finite width of these contours reflects drop oscillations, which in Thurai and Bringi (2005) were quantified in terms of the mean and width of the axis ratio distributions. To give an indication of the inferred

oscillation amplitudes, for the 4–4.25-mm drops, the maximum horizontal chord was within 3.8 and 4.9 mm for 95% of the cases while the vertical chord was within 2.6 and 4.1 mm. The most probable dimensions were 3.4 mm for the vertical and 4.4 mm for the horizontal, giving a mean axis ratio of 0.77.

Each image in Fig. 1 has two curves superimposed on it. The one in black represents our estimate of the best-fitted equation to the most probable contour, given by

$$x = c_1 \sqrt{1 - \left(\frac{y}{c_2}\right)^2} \left[\cos^{-1}\left(\frac{y}{c_3 c_2}\right)\right] \left[c_4 \left(\frac{y}{c_2}\right)^2 + 1\right],$$

(1)

where $x$ and $y$ are the Cartesian coordinates and the parameters $c_1$, $c_2$, $c_3$, and $c_4$ were fitted to obtain the mean dependence on the equivolumetric sphere diameter ($D_{eq}$ in mm), given by

$$c_1 = \frac{1}{\pi}(0.02914 D_{eq}^2 + 0.9263 D_{eq} + 0.07791),$$

$$c_2 = -0.01938 D_{eq}^2 + 0.4698 D_{eq} + 0.09538,$$

$$c_3 = -0.06123 D_{eq}^3 + 1.3880 D_{eq}^2 - 10.41 D_{eq} + 28.34,$$

$$c_4 = -0.01352 D_{eq}^3 + 0.2014 D_{eq}^2 - 0.8964 D_{eq}$$

$$+ 1.226 \quad \text{for} \quad D_{eq} > 4 \text{ mm},$$

$$c_4 = 0 \quad \text{for} \quad 1.5 \text{ mm} \leq D_{eq} \leq 4 \text{ mm}.$$

The form of (1)[1] is a modification of the mathematical formulation representing smooth conical-like shapes given in Wang (1982; $c_1$, $c_2$, and $c_3$ are the same as the parameters $a$, $c$, and $\lambda$ in that reference). The last bracketed term containing $c_4$ is the only modification to the Wang formula that had to be introduced to get a more precise fit to the most probable contour for drops larger than 4 mm. Fitting of the other three parameters ($c_1$, $c_2$, and $c_3$) is similar to that given in Wang et al. (1987).

The second superimposed curve in Fig. 1, shown in blue, represents the approximated oblate spheroid shape with axis ratio given by a refitted formula to the measurements reported in Thurai and Bringi (2005) for $D_{eq} > 1.5$ mm:

$$\frac{b}{a} = 1.065 - 6.25 \times 10^{-2}(D_{eq}) - 3.99$$

$$\times 10^{-3}(D_{eq}^2) + 7.66 \times 10^{-4}(D_{eq}^3)$$

$$- 4.095 \times 10^{-5}(D_{eq}^4),$$

(2)

where the ratio $b/a$ represents the minor to major axis ratio for the equivalent oblate spheroid. This refitted formula is a much closer representation of the axis ratio measurements for all $D_{eq}$ values ranging from 1.5 up to 10 mm.

Figure 1 clearly shows that the larger drops have more deviation from oblate spheroid shapes. The 3–3.25- and 4–4.25-mm drop contours agree closely with the approximated formula in (2) above whereas the 5–5.25- and 6–6.25-mm drop contours show more deviation, clearly with a much flatter base. As shown later, these deviations can have some effect on differential reflectivity calculations for certain regimes of drop size distributions.

## 3. Comparison with Beard–Chuang (nonoblate shape) model

The full numerical model of Beard and Chuang (1987) (B–C), although often approximated to oblate spheroids for practical applications, in actual fact predicts shapes that are similar to those in Fig. 1. Their model computation results in "a singly curved surface with a flattened base and a maximum curvature just below the major axis," a feature that could also be noticed in Fig. 1d for the 6-mm drops. The B–C model shapes were given in terms of a summation of cosine series, the coefficients of which are given in Table 4 of their article. These coefficients were used to derive the mean drop shapes for the four drop diameters considered in Fig. 1; the comparisons are given in Fig. 2. As seen, the B–C model results lie close to the measured probability contours, although the latter show a slightly more flattened base for the larger drops. This minor discrepancy increases slightly for larger drop diameters (7–8 mm; not shown here).

The other (nonoblate shape) model often quoted in the literature is the Pruppacher and Pitter (1971) model (P–P). When compared with the B–C model, it produces a noticeable indentation at the base for drop diameters above 5 mm. Such indentations were not immediately obvious in our contours, even for the largest diameters examined (up to 9 mm). It has been noted earlier that drops in the 7–9-mm region showed a slight decrease in their mean fall velocities (Thurai and Bringi 2005), attributed to a possible increase in drop distortion giving rise to an increase in drag when compared with the increase in weight. Nevertheless, since the B–C model gives good agreement with our measured contours, we would expect their above-mentioned statement on the "singly curved surface with a flattened base" to apply to large drops.

## 4. Calculations of polarization variables

In previous studies, the P–P (nonoblate shape) model has been used for scattering calculations to quantify the effect of the equivalent oblate approximation (Oguchi 1977; Morgan 1980). We consider here the consequences of our measured shapes on scattering ampli-

---

[1] Equation (1) has also been shown to be valid for drop shapes in natural rain (Thurai et al. 2006), at least for 1.5 mm $\leq D_{eq} \leq 4$ mm; the upper limit of 4 mm was only restricted because of an insufficient number of larger drops in natural rain to derive statistically meaningful probability contours.
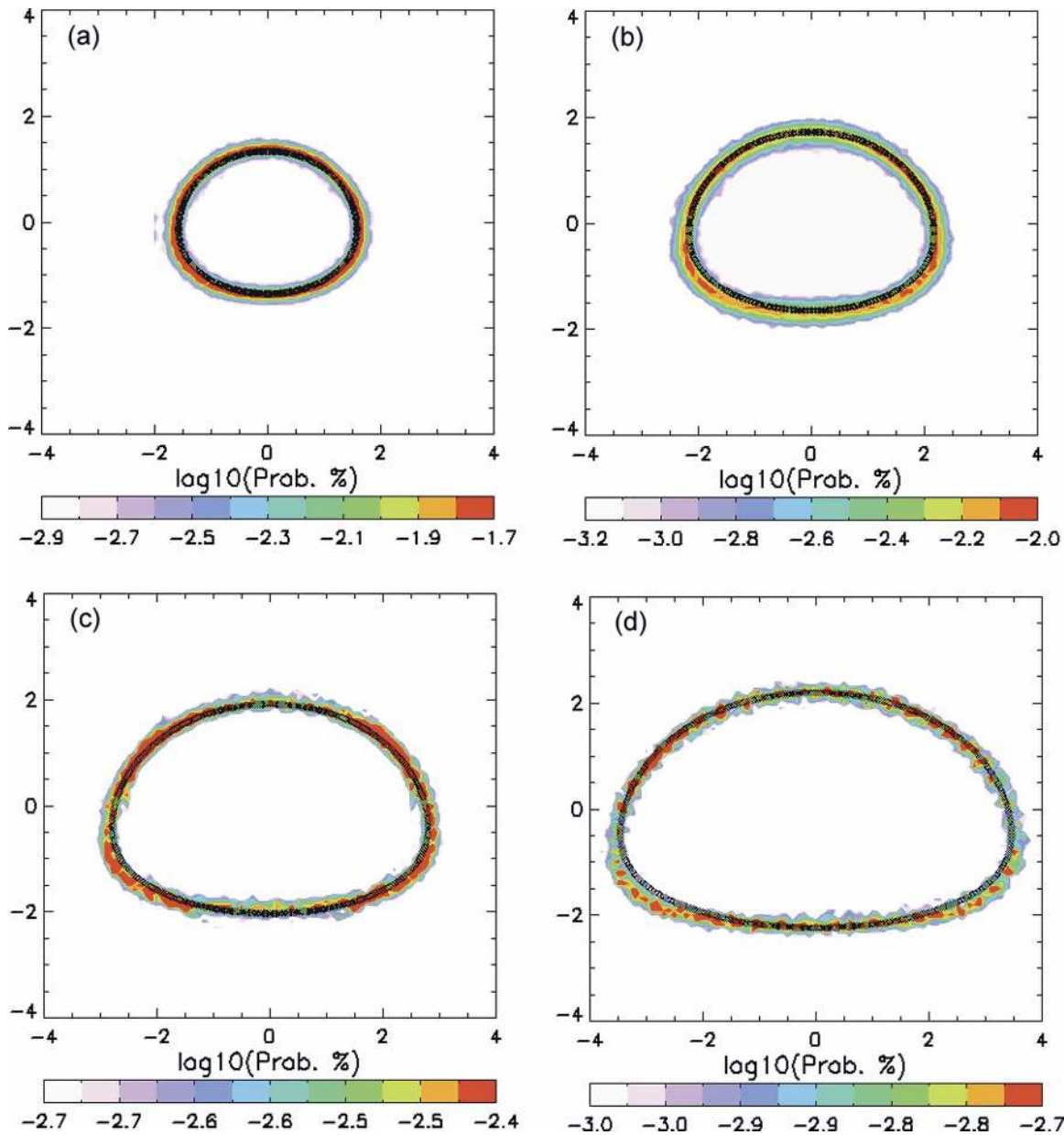
FIG. 2. The same probability contours as in Fig. 1, but compared with the Beard and Chuang (1987) shapes (shown in black) derived using Table 4 of their paper.

tudes and extend the considerations to examine the effect on radar polarization parameters as well.

*a. C-band scattering calculations: Single particles*

Using (1) for the mean drop shapes, the complex scattering amplitudes for forward and backscatter were calculated using the T-matrix method. Table 1 shows the calculations at 5.34 GHz (C band) for $D_{eq}$ larger than 1.5 mm. The computations correspond to 20°C water temperature and the dielectric constant from Ray

(1972). Figure 3a compares these calculations with the Mie solutions for spheres in terms of the normalized backscatter cross section (i.e., normalized with respect to the cross-sectional area). The Mie curve lies in between the horizontal (H) and vertical (V) polarization curves but for $D_{eq}$ up to 5.5 mm, it lies somewhat closer to the former. The resonance effects (e.g., Keenan et al. 2001) are evident in the 5.5–7-mm region in all three cases. Note also in this region, the difference between H and V cross sections is the greatest.

TABLE 1. Real and imaginary parts of the complex scattering amplitudes (in m) for H and V polarizations at C band as a function of drop equivolumetric sphere diameter.

| Diameter (mm) | Real, forward for V | Imaginary forward for V | Real, forward for H | Imaginary forward for H | Real, back for V | Imaginary back for V | Real, back for H | Imaginary back for H |
|---|---|---|---|---|---|---|---|---|
| 1.75 | 8.2682E-06 | −1.5864E-07 | 8.6830E-06 | −1.7120E-07 | 7.8330E-06 | −2.3357E-08 | −8.2287E-06 | 2.9511E-08 |
| 2 | 1.1974E-05 | −2.6310E-07 | 1.2961E-05 | −2.9624E-07 | 1.1147E-05 | −3.6658E-10 | −1.2073E-05 | 1.2505E-08 |
| 2.5 | 2.2496E-05 | −6.6636E-07 | 2.5770E-05 | −8.0770E-07 | 2.0026E-05 | 1.6217E-07 | −2.2971E-05 | −1.4593E-07 |
| 3 | 3.8154E-05 | −1.5582E-06 | 4.6172E-05 | −2.0287E-06 | 3.1984E-05 | 6.6554E-07 | −3.8757E-05 | −7.2297E-07 |
| 3.5 | 6.0382E-05 | −3.4459E-06 | 7.7267E-05 | −4.8663E-06 | 4.6748E-05 | 1.9384E-06 | −5.9781E-05 | −2.4108E-06 |
| 4 | 9.1026E-05 | −7.3393E-06 | 1.2361E-04 | −1.1489E-05 | 6.3491E-05 | 4.8696E-06 | −8.5591E-05 | −6.9997E-06 |
| 4.5 | 1.3556E-04 | −1.5939E-05 | 1.9512E-04 | −2.8498E-05 | 8.1989E-05 | 1.1841E-05 | −1.1541E-04 | −2.0264E-05 |
| 5 | 1.9821E-04 | −3.5091E-05 | 3.0202E-04 | −7.5620E-05 | 9.9309E-05 | 2.8289E-05 | −1.4696E-04 | −6.0450E-05 |
| 5.5 | 2.8179E-04 | −7.8043E-05 | 4.2854E-04 | −2.0655E-04 | 1.1349E-04 | 6.6800E-05 | −2.0527E-04 | −1.7844E-04 |
| 6 | 3.7528E-04 | −1.7006E-04 | 4.2895E-04 | −4.2227E-04 | 1.3500E-04 | 1.5161E-04 | −4.4403E-04 | −3.6993E-04 |
| 6.5 | 4.2434E-04 | −3.2713E-04 | 3.3183E-04 | −4.6120E-04 | 2.1508E-04 | 2.9718E-04 | −8.3719E-04 | −3.6372E-04 |
| 7 | 3.6672E-04 | −4.7530E-04 | 3.8483E-04 | −4.1557E-04 | 4.0899E-04 | 4.2759E-04 | −1.1290E-03 | −2.3575E-04 |
| 7.5 | 2.6574E-04 | −5.2453E-04 | 5.3563E-04 | −4.3320E-04 | 6.6292E-04 | 4.4670E-04 | −1.3772E-03 | −9.6335E-05 |
| 8 | 2.2212E-04 | −5.0920E-04 | 7.0618E-04 | −5.3560E-04 | 8.7525E-04 | 3.7906E-04 | −1.6015E-03 | 6.2197E-05 |
| 8.5 | 2.3500E-04 | −5.0400E-04 | 8.4900E-04 | −6.6600E-04 | 1.0300E-03 | 2.9100E-04 | −1.7800E-03 | 1.9300E-04 |
| 9 | 2.6400E-04 | −5.2600E-04 | 1.0300E-03 | −7.8400E-04 | 1.1300E-03 | 2.1200E-04 | −1.9900E-03 | 2.5200E-04 |

Figure 3a also shows the normalized backscatter cross sections calculated using (2). In general, they agree well with those using (1), but in the 6-mm region, the equivalent oblate spheroid approach slightly underestimates the backscatter cross section for H polarization and slightly overestimates for V polarization. The effect of this discrepancy is more evident in Fig. 3b,

which compares the equivalent $Z_{dr}$ values derived for the two cases. In the 6–7-mm region, the contoured shapes give 0.5 dB higher $Z_{dr}$ than the equivalent oblate spheroid shapes. For smaller and larger diameters, the differences are negligible. The shape effects on $Z_{dr}$ are mostly negligible except in the resonance region.
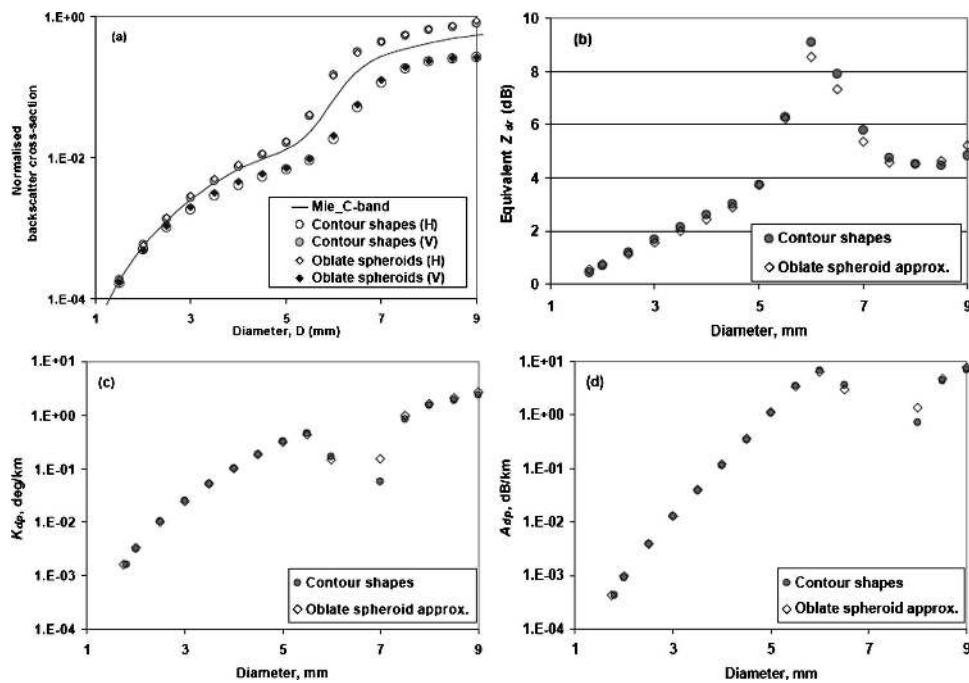
The resonance effect in the 5.5–7-mm region also



FIG. 3. (a) Comparisons of normalized backscatter cross sections for H and V polarizations using the contoured shapes [Eq. (1)] and the approximated oblate spheroids [Eq. (2)]. (b) Comparisons of single particle $Z_{dr}$. (c) Comparisons of single particle $K_{dp}$ assuming a drop concentration of 1 per m$^3$. (d) Comparisons of single particle $A_{dp}$ assuming the same drop concentration.

affects the specific differential phase ($K_{dp}$) and the specific differential attenuation ($A_{dp}$) at C band. The $K_{dp}$ depends on the real part of the difference between the forward scattering amplitudes at H and V polarizations, while $A_{dp}$ depends on the corresponding difference of the imaginary parts. As deduced from Table 1, these differences are positive for all diameters except for the 6.5-mm case. This trend is also predicted by the oblate spheroid approximation, although some differences in their magnitudes were observed, once again in the 6–7-mm region. The single particle $K_{dp}$ and $A_{dp}$ are given in Figs. 3c and 3d, assuming a concentration of 1 particle per cubic meter. Negative values in the 6–7-mm region are not shown (since the $y$ axes are on log scales), but they agree with prior calculations at C band (e.g., Keenan et al. 2001).

### b. C-band scattering calculations: Integration over DSD

Having compared the radar and propagation parameters for individual drops, we now examine the integrated effect over a range of drop size distributions, both measured as well as model-based.

#### 1) CALCULATIONS USING MEASURED DSDs

For the measured DSDs, a previously analyzed event (Bringi et al. 2006) in an oceanic, subtropical location (Okinawa, Japan) is used here. This was a long duration baiu event that lasted over 12 h and had rainfall rates up to 100 mm h$^{-1}$, but the size of drops as measured with the 2DVD rarely exceeded 5 mm (as shown in Figs. 12, 14, and 16 of Bringi et al. 2006).

T-matrix calculations were performed for the 1-min integrated DSDs from this event. The DSDs were fitted to normalized gamma distributions using the method described in Bringi et al. (2003). The maximum diameter for the size integration was set to a "realistic" value of 3 times the estimated median volume diameter ($D_0$) corresponding to each of the DSDs or set at 8 mm, whichever was less. The water temperature was set to 20°C and a Gaussian canting angle distribution with zero mean and 5° standard deviation was used to account for turbulence effects. The overall effects of the contoured shapes are given in Fig. 4, in terms of the various radar parameters at C band. It shows the comparisons between the T-matrix calculations based on the contoured shapes using (1) and their oblate approximations using (2). Note that in both sets of calculations, a fitted formula for drops smaller than 1.5 mm to the more accurate laboratory measurements of Beard and Kubesh (1991) was used, given by

$$\frac{b}{a} = 1.173 - 0.5165(D_{eq}) + 0.4698(D_{eq}^2) - 0.1317(D_{eq}^3)$$

$$- 8.5 \times 10^{-3}(D_{eq}^4) \quad \text{for} \quad 0.7 \leq D_{eq} \leq 1.5 \text{ mm.}$$

(3)

Below 0.7 mm, drops were assumed spherical, again for both sets of calculations.

Six parameters were computed, namely, (a) $Z_H$, (b) $Z_{dr}$, (c) $K_{dp}$, (d) $A_H$, (e) $A_{dp}$, and (f) the linear depolarization ratio (LDR), for C band (5.34 GHz). Figure 4 shows close agreement between the calculations using the most probable shapes and those derived using the equivalent oblate spheroids. Over 1600 one-minute DSDs are represented in the figure. Although they represent rainfall rates ranging up to 100 mm h$^{-1}$, over 80% of the cases have rain rates less than 10 mm h$^{-1}$. Hence, the DSD data are weighted toward the stratiform, less intense periods of the event (Bringi et al. 2006). Nevertheless, as seen in Fig. 4, agreement to within a few percent is obtained even for the higher values of rainfall rates for all computed parameters. For example, for the highest recorded rainfall rate of 102 mm h$^{-1}$, the computed values for $Z_H$, $Z_{dr}$, $K_{dp}$, $A_H$, and $A_{dp}$ were 53.1 dB$Z$, 4.3 dB, 5.46° km$^{-1}$, 0.328 dB km$^{-1}$, and 0.111 dB km$^{-1}$, respectively for case using (1), compared with 53.0 dB$Z$, 4.0 dB km$^{-1}$, 5.54° km$^{-1}$, 0.35 dB km$^{-1}$, and 0.109 dB km$^{-1}$ using the approximated oblate spheroid approach. These comparisons represent small errors (<4%). This is not surprising, given the fact that the maximum drop sizes observed during this event rarely exceeded 5 mm. As seen earlier in Fig. 3, noticeable deviation from oblate shapes only occurs within the resonance region for $D_{eq}$ in the 5.5–7-mm range at C band.

Thurai and Hanado (2005) as well as Bringi et al. (2006) have used the measured DSDs from the baiu front event to examine the validity of the so-called $\Phi_{dp}$ consistency method at C band for attenuation correction and radar external calibration. Analyses using PPI scans of $Z_H$, $Z_{dr}$, and $K_{dp}$ taken over 8 h showed that it was possible to determine the reflectivity calibration factor as well as to quantify the effects due to rain-on-radome. The method used the approximated oblate spheroids for deriving the various relationships required for the attenuation-correction scheme and the subsequent reconstruction of the differential phase profiles. These relationships entailed the five parameters shown in Figs. 4a–e. Since our comparisons show that the oblate approximation is sufficiently accurate for deriving these five parameters for this event, we would expect the same relationships to apply for the con-
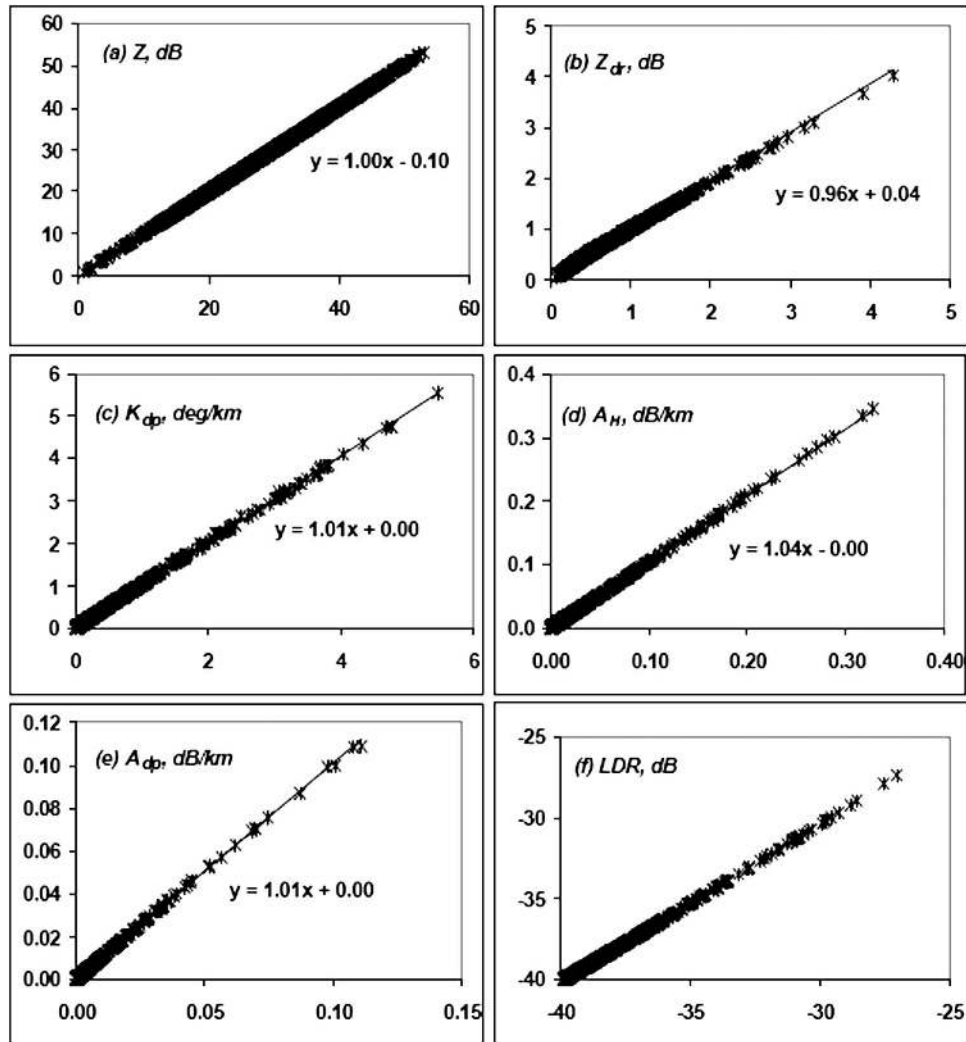
FIG. 4. Comparisons of (a) $Z_H$, (b) $Z_{dr}$, (c) $K_{dp}$, (d) $A_H$, (e) $A_{dp}$, and (f) LDR using the contoured shapes ($x$ axis) and the approximated oblate spheroids ($y$ axis). For the first five parameters, equations for the best fitted lines are given.

toured shapes and hence no change would be required for that event analysis.

### 2) CALCULATIONS FOR MODEL DSDs

The DSDs used in the above calculations were obtained in a subtropical environment during a particular rainy event (i.e., the baiu front in Okinawa, as mentioned earlier). In this section, we examine how the DSDs in other climatic regimes would affect the comparisons between the true shapes and the approximated oblate spheroids. To this end, distributions of DSDs representing 1) continental convective and 2) tropical convective rain regimes were generated. The DSDs were based on the normalized gamma distribution characterized by the normalized intercept parameter ($N_w$ in

$mm^{-1}\ m^{-3}$), the median volume diameter ($D_0$ in mm), and the shape factor ($\mu$). For case 1, values of $\log_{10}(N_w)$ used were in the range $3.37 \pm 0.52$, $D_0$ in the range $2.3 \pm 0.52$ mm, and $\mu$ in the range $2.35 \pm 2.08$. For case 2, the corresponding ranges were $4.27 \pm 0.43$, $1.58 \pm 0.36$, and $3.4 \pm 2.3$, respectively. These values were obtained from previously published studies (Bringi et al. 2003, their Fig. 11) and are given here in Table 2. Over 2000 DSDs were generated for each of the two cases, with rainfall rates exceeding 100 mm $h^{-1}$ for 20% of the cases for rain type 1, and 10% of the cases for rain type 2. The DSD parameters were uniformly distributed within their respective ranges. Other input parameters for the T-matrix calculations were kept the same as before.

TABLE 2. Range of values for the gamma DSDs used as input to the T-matrix calculations.

| Case | $\log_{10}(N_w)$ | $D_0$ | $\mu$ |
| --- | --- | --- | --- |
| 1 | $3.37 \pm 0.52$ | $2.3 \pm 0.52$ | $2.35 \pm 2.08$ |
| 2 | $4.27 \pm 0.43$ | $1.58 \pm 0.36$ | $3.4 \pm 2.3$ |

The resulting comparisons are shown only for $Z_{dr}$ since the other radar parameters were found not to be affected by the shape difference between contoured and oblate (as was the case discussed earlier using the measured DSDs). Figure 5 shows $\Delta Z_{dr} = Z_{dr}$ (oblate) $- Z_{dr}$ (most probable contoured) versus $D_0$ for DSD cases 1 and 2, as well as the measured DSDs from the baiu front event. The errors are within $\pm 0.1$ dB for $D_0 < 2$ mm whereas for larger $D_0$ values, a trend is observed where the oblate approximation shows a bias of up to $-0.3$ dB. For the tropical convective case (case 2) and the measured DSDs, $\Delta Z_{dr}$ were largely negligible, owing to the smaller $D_0$ and hence the lack of drops in the resonance region. The effect of increasing $D_{max}$—the maximum diameter over which the integration is performed—was also examined, but this did not affect the resulting comparisons significantly. Apart from $Z_{dr}$, other radar parameters remain unaffected by the nonoblate shapes (errors are not shown here).

## c. Calculations at S and X bands

We now consider the drop shape effects at two other radar frequency bands, namely, S and X bands. For S band, it is well known that resonances occur at 12–15 mm, which is outside the range of raindrop sizes, whereas for X band the resonance occurs in the 3–4-mm range, but the higher absorption dampens the resonance effect when compared with C band. Similar to
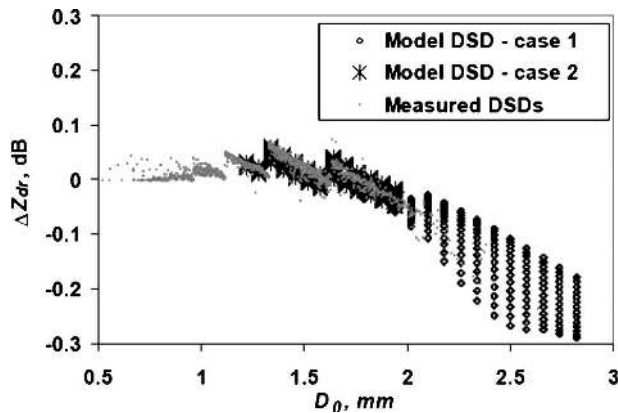
Fig. 3b, the single particle $Z_{dr}$ comparisons between oblate and contoured shapes are shown in Figs. 6a and 6b for S band and X band, respectively. As in the C-band case, the differences are essentially negligible except near the resonance region, which is apparent/relevant only for X band. The other important polarimetric parameters, $K_{dp}$ and $A_{dp}$, showed negligible shape differences (thus not shown here).

The integrated effect over the whole DSD ranges for the two model-based cases and the measured baiu front case was examined for all parameters. Here we show the effect on $Z_{dr}$, similar to Fig. 5 earlier for C band. Figures 7a and 7b shows the $\Delta Z_{dr}$ versus $D_0$ for S band and X band, respectively. The biases are smaller compared with C band, the highest values being $-0.15$ dB at S band and $-0.2$ dB at X band. Because of the systematic nature of the error, the most probable shapes are recommended for the $Z_{dr}$ calculations for DSDs with relatively high $D_0$ values ($>2.5$ mm), while the other parameters can be derived using their oblate approximations.

Unusual DSDs with large $D_0$ values exceeding 3–4 mm have been observed, for example, along the leading
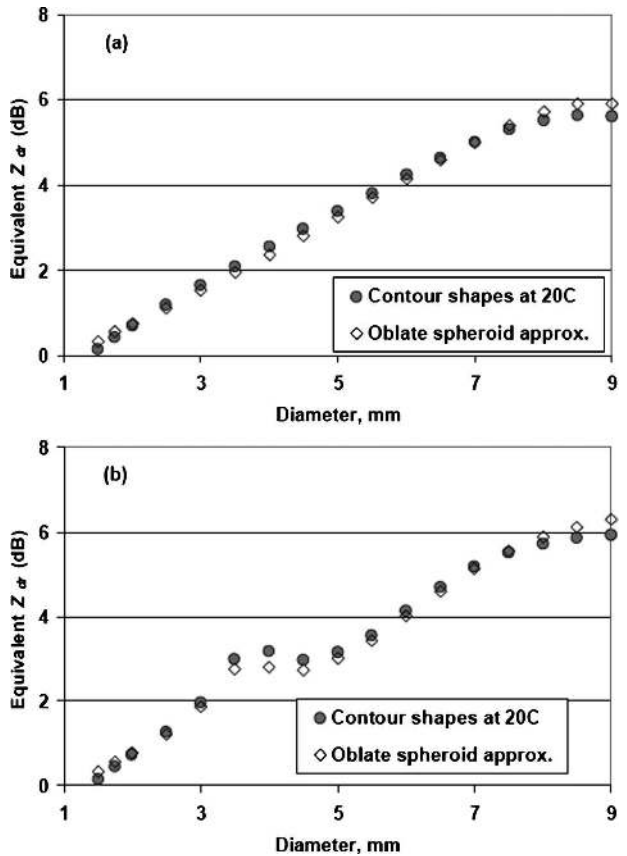


FIG. 5. $\Delta Z_{dr} = Z_{dr}$ (oblate) $- Z_{dr}$ (most probable contoured) vs $D_0$ for DSD cases 1 and 2, as well as the measured DSDs, calculated at 20°C.



FIG. 6. Comparisons of single particle $Z_{dr}$ for (a) S band and (b) X band.

FIG. 7. $\Delta Z_{dr}$ vs $D_0$ for the same DSDs as in Fig. 5, calculated at 20°C for (a) S band and (b) X band.



FIG. 8. $\Delta Z_{dr}$ vs $D_0$ for the same DSDs as in Fig. 5, calculated at 1°C for C band.

based DSD cases 1 and 2 as well as the measured DSDs indicate the same conclusions as before; that is, the oblate shape approximation generally applies. The $Z_{dr}$ biases due to shape effects were found to reduce with decreasing temperature. Figure 8 shows the $\Delta Z_{dr}$ versus $D_0$ for temperature of 1°C. Compared with the 20°C case in Fig. 5, the biases are generally smaller, for $D_0 > 2$ mm, the largest bias being $-0.2$ dB.

## 5. Conclusions

Drop shapes derived from the fast line-scanning cameras of a two-dimensional video disdrometer are presented in terms of probability contours. They indicate that the shapes begin to deviate from oblate spheroids for drop diameters larger than 4–5 mm, the larger drops having more flattened base, in good agreement with the equilibrium (nonoblate) shape model of Beard and Chuang (1987). Deviations from the B–C model shapes were found for diameters larger than 6 mm, but overall the 2DVD data from the 80-m fall experiment are the first demonstration of the good agreement between the most probable contoured shapes and the B–C model shapes for large drops.

The measured contours were fitted to a modified conical equation with four parameters to represent the most probable shapes. Scattering calculations were performed using the T-matrix method to derive the complex scattering amplitudes for forward and backscatter for H and V polarizations at C band. The normalized backscatter cross sections were compared with the equivalent Mie theory for spherical shapes. Beyond 5 mm, the H and V polarization curves lie on either side of the Mie curve while below 5 mm, the H-polarization curve lies close to the Mie curve. Resonance effects are

edge of severe convective cells (Schuur et al. 2001) with accompanying low rain rates. Ryzhkov and Zrnić (1995) also report on such unusual DSDs causing excessive attenuation at S band in Oklahoma convective storms and attributed to giant rain drops. Very large $Z_{dr}$ values (6–8 dB) have also been observed at C band (Meischner et al. 1991; Carey et al. 2000) due to "big drops." In such cases we would expect more differences in the radar parameters between the contoured shapes and the approximated oblate spheroids.

### d. Temperature effects

The effect of drop temperature (via the dielectric constant) on polarimetric radar parameters has been studied extensively using oblate shapes (e.g., see Bringi and Chandrasekar 2001, chapter 7 and references therein). Notable are the temperature effects on $Z_{dr}$ and on specific attenuation, with much less effect on $K_{dp}$ and $A_{dp}$, especially at C band (e.g., Keenan et al. 2001).

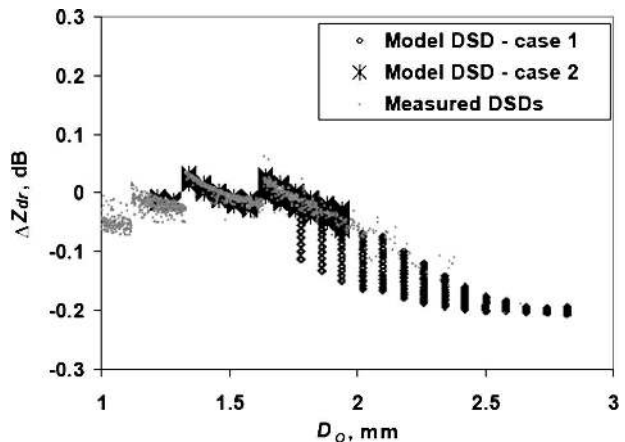C-band calculations at other temperatures for model-

visible in the 5.5–7-mm region. Computations of single particle $Z_{dr}$, $K_{dp}$, and $A_{dp}$ using an equivalent oblate spheroid shape approach show good agreement with those using the contour shapes except within the resonance region.

Calculations were made at C band using the contour shapes to derive $Z_H$, $Z_{dr}$, $K_{dp}$, $A_H$, and $A_{dp}$ for over 1600 one-minute DSDs measured during a subtropical rain event. These were compared with the corresponding calculations using approximated oblate spheroid shapes. Agreement for all five parameters except $Z_{dr}$ was good for this event, which was characterized by maximum drop sizes no more than 5 mm. The $Z_{dr}$ showed a slight underestimation when using the oblate spheroid approximation.

Calculations were also made for model DSDs based on gamma distributions, the parameters for which were chosen to represent (case 1) continental convective and (case 2) tropical convective rain regimes. For the continental convective rain case, with its $D_0$ values ranging up to 2.8 mm, the approximated oblate spheroid calculations tended to systematically underestimate $Z_{dr}$ values by up to −0.3 dB. The effect of increasing $D_{max}$ was also examined but this did not significantly affect the results.

Single particle calculations at S and X bands show similar comparisons to C band; that is, $Z_{dr}$ is the only parameter that is affected by the oblate shape approximation mainly in the resonance region at X band (3.5–5 mm). Integration over the various DSD cases showed a systematic underestimation for $Z_{dr}$ when using the oblate shapes for the larger $D_0$ values (up to −0.15 dB at S band and −0.2 dB at X band).

Calculations were also performed at C band for the full range of DSDs at temperatures of 1° and 20°C. The temperature effects on $Z_{dr}$ were such that at lower temperatures, closer $Z_{dr}$ agreement between the contoured shapes and the oblate approximations were found even for larger $D_0$ values, mainly because at lower temperatures the higher absorption tends to dampen the resonance effects.

Our calculations of $Z_{dr}$ using the most probable contoured shapes versus the equivalent oblate shapes show that at S band the oblate approximation is sufficient even for DSDs with large $D_0$ values (up to around 3 mm). At C band we recommend that for high accuracy the use of the most probable contoured shapes be used, especially for $D_0$ values >2.5 mm, since the oblate approximation systematically underestimates $Z_{dr}$ by up to −0.3 dB. At X band the underestimation is in between the S- and C-band values and the oblate approximation appears to be sufficient even for large $D_0$ values (up to around 3 mm). We note, however, that unusual DSDs with very large $D_0$ values (>3 mm) can accentuate the difference between the contoured shape and the oblate spheroid equivalent, for example, as can occur along the leading edge of severe convective cells or aloft due to "big drop" zones inferred for example by Ryzhkov and Zrnić (1995) and measured by Schuur et al. (2001) at S band, and inferred by Meischner et al. (1991) and Carey et al. (2000) at C band.

Our calculations support the oblate spheroid shapes using a composite of axis ratio versus $D$ relations given by (2) and (3) that covers the range $0.7 < D < 8$ mm. In particular, this is sufficient to derive the various $K_{dp}$-based attenuation-correction schemes and the subsequent rainfall estimation at S, C, and X bands.

## APPENDIX

### Contour Smoothing of 2DVD Hydrometeor Image Data

The 2DVD cameras record the front and side view shadow contours of each hydrometeor falling through the sensor area with a resolution fine enough to result in negligible quantization errors for both drop cross sections and drop volumes. However, the quantization effects can play a role in the determination of drop canting angle and hence a suitable contour smoothing algorithm needed to be developed and implemented.

Careful analyses of various methods suggested that the contour smoothing algorithm should be based on the following principles: the 2DVD data describe a particle's contour using a run length code, indicating start and end of shadow for each scan line. The quantization introduced by the pixel size (about 0.2 mm in the horizontal as well as in the vertical) causes an uncertainty range, represented by appropriately selected control points on its inner and outer boundary. After applying standard polygon smoothing techniques on the inner and outer set of control points, the smoothed shape of the particle is obtained in terms of the weighted means of the inner and outer smoothed uncertainty range boundaries. Weighting coefficients are found from calibration sphere comparisons; they deviate only marginally from the 50% mean of inner and outer boundary vectors.
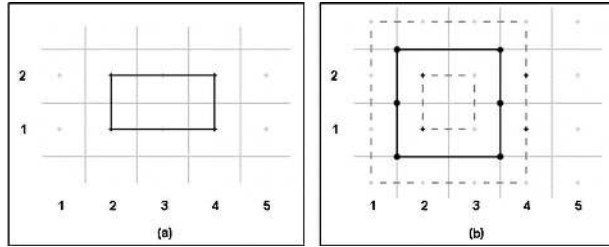
FIG. A1. (a), (b) Illustration of 2DVD data representing an object passing through the measuring area and shadowing an area of $2 \times 2$ pixels for two line scan periods. The first shadowed and the first nonshadowed pixel of each scan line is marked by a black cross. Whereas (a) immediately follows from the run length code information provided by the 2DVD, (b) shows processed data indicating the uncertainty boundaries (dashed) and their 50% mean (= best possible estimate of true shadow contour).
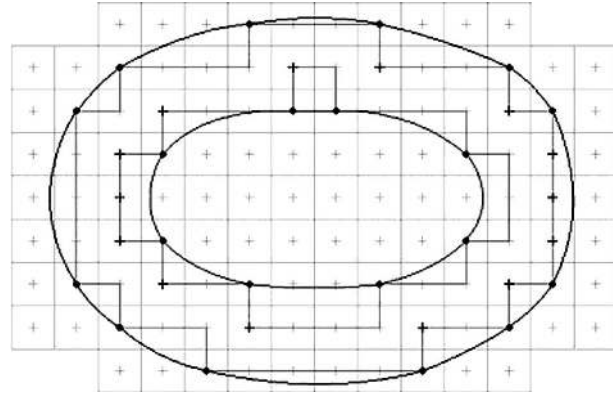


FIG. A2. View of an oblate spheroid. The light gray lines represent the digitizing grid; black crosses indicate the run length coded transitions; straight gray lines show inner and outer boundary of uncertainty range; their control points are shown as black dots. The solid lines represent the smoothed contour (method explained below) of control points.

## a. 2DVD data type

The 2DVD employs two line scan cameras, with data preprocessed so that the user obtains the information on whether or not a specific camera pixel at a certain time was shadowed. At typical rain drop fall velocities ($<10$ m s$^{-1}$), this results in a grid resolution finer than 0.2 mm, leaving a small uncertainty range in which the true shadow contour could lie. For illustration, Fig. A1 shows a sample of an object (e.g., a cube falling through the measuring area) shadowing exactly two pixels for the duration of two line scan periods. A camera pixel grid is indicated by gray lines and the pixel centers are marked by crosses. The black crosses indicate transitions from illuminated to shadowed line portions (first illuminated pixel) or vice versa (first shadowed pixel). Whereas Fig. A1a reflects an outline immediately following from the run length code generated by the 2DVD, Fig. A1b shows the inner and outer uncertainty boundaries as dashed lines and their 50% mean indicated by the solid black line, the latter providing the best possible estimate of the simple $2 \times 2$ pixels sample object's true contour.

## b. Control points on uncertainty range boundaries

The inner and outer boundaries of uncertainty range are polygons with horizontal or vertical edges. These polygons generally have both inward (concave) and outward (convex) pointing corners even for a fully convex object like an oblate spheroid. As control points, the outward pointing corners of the outer boundary and the inward pointing ones of the inner boundary are chosen.

Figure A2 gives an illustration: the gray lines represent the digitizing grid, the black crosses mark the transition pixels, and the straight light-gray lines indicate inner and outer boundaries of the uncertainty range. The black dots are the control points chosen on the outer and inner boundaries.

In principle, the method has been formulated and implemented for particles with concave sections in their silhouette also (e.g., irregularly shaped hailstones and snowflakes). However, satisfactory results are usually obtained for particles with purely convex silhouettes only, such as those of raindrops.

## c. Smoothed contour of control point sets

Having obtained the sets of control points, standard contour smoothing techniques are applied. Relevant literature describes a variety of algorithms, most of them offering specific advantages and disadvantages depending on the problem to be solved. As a basic criterion, discrimination between approximation and interpolation methods is made, determining if the set of points to be connected by a smooth contour is to be part of the resulting curve (interpolation) or just close to it (approximation).

In practice, a closed curve is normally made up of several segments. Therefore, it is important to consider the way these segments are connected at the joining points. Generally speaking a curve provides $n$th-order parametric continuity $C_n$ at a point $P$, if the first $n$ derivatives of the two segments, connected at $P$, match at this point.

Table A1 lists standard image processing methods implemented and evaluated for 2DVD contour smoothing. Validity comparisons performed include cross-checks of canting angle results against known

TABLE A1. Methods evaluated for 2DVD contour smoothing.

| Approximation methods | Interpolation methods |
| --- | --- |
| Bézier curves | Lagrange interpolation |
| B splines | Akima interpolation |
| Nonuniform rational B splines (NUBRS) | |

mean canting angles. An experiment with artificial rain and the instrument being tilted by a known angle had provided the required dataset.

For brevity, a detailed report on the various evaluations is omitted here: finally the Akima interpolation method was chosen for the 2DVD application.

The Akima interpolation method is characterized by the following properties.

- The interpolants have first derivative continuity ($C_1$) at the data points.
- Only four coefficients have to be solved for, and therefore this interpolation method is computationally efficient.
- The Akima interpolation is a "local" method, which means that the value at any point of the interpolant depends only on data in the immediate neighborhood of the point.
- Because no functional form for the whole curve is assumed and only a small number of points are taken into account, this method does not lead to unnatural "wiggles."

### d. The 50% mean of smoothed uncertainty range boundaries

To determine the average between the inner and outer smoothed uncertainty range boundaries, the following steps are performed.

- Both inner and outer curves are divided into small linear segments by determining N equidistant points $P_i$ (in) on the inner curve and $N$ equidistant points $P_i$ (out) on the outer curve (Fig. A3). Since the number of the linear segments defines the smoothness of the resulting contour approximation, $N$ must not be chosen to be too small.
- The centroid $P_C$ of the inner curve is obtained in a straightforward manner.
- Next, the points $P_i$ of the averaged curve are determined. By coordinate geometry calculations, for each of the $N$ rays from $P_c$ to the $N$ points $P_i$ (out) the intersection point $P_i$ (in)′ with the inner smoothed uncertainty range boundary is determined. For each index $i$ the requested point $P_i$ is found as vectorial mean of $P_i$ (out) and $P_i$ (in)′.
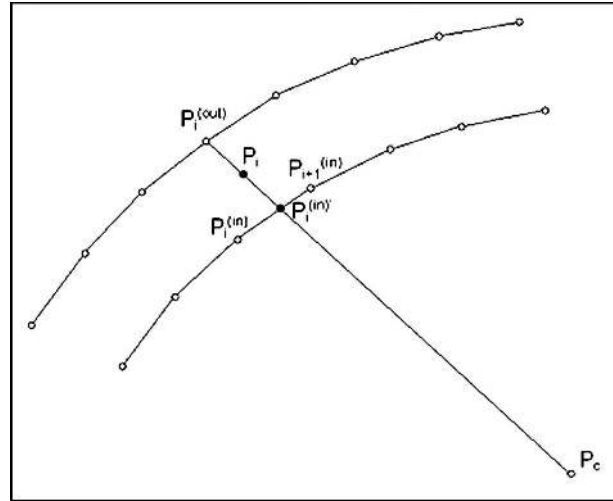


FIG. A3. Determining 50% mean of inner and outer uncertainty range boundary. First, the point $P_i$ (in)′ is found from the intersection between the line $P_c$ to $P_i$ (out) and the line between the two adjacent points $P_i$ (in) and $P_{i+1}$ (in) of the inner curve.

- Finally, all points $P_i$ are connected with straight lines. The smoothness of the resulting contour increases with the number $N$, but so does the computing time as well. Hence, $N$ has to be determined as a compromise between these two considerations.

### e. Calibration spheres crosschecks and weighted mean

Having obtained a contour smoothing algorithm producing plausible graphical quality, the effect on the ba-
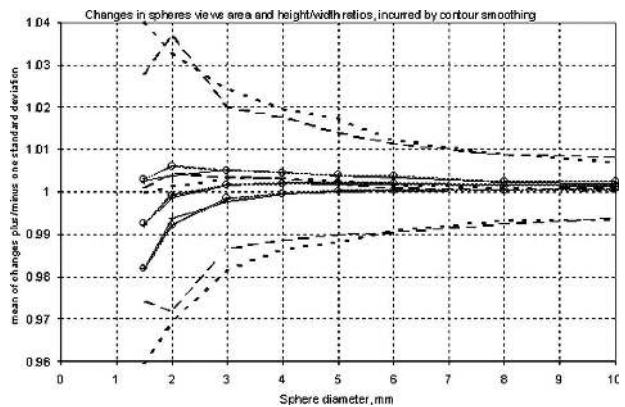


FIG. A4. The effect of the contour smoothing algorithm onto area and height/width ratio of calibrations spheres' silhouette views. The solid lines with crosses apply to camera A and indicate the mean values and their ± standard deviations for quotients of the smoothed contour's area divided by the area values directly derived from measurements (shadowed pixels). Gray lines with circles give the same for camera B. The dashed lines represent height/width ratios in camera A, and the dotted lines stand for height/width ratios in camera B. All mean values deviate less than 1% from unity.

sic parameters *of the silhouette views*, that is, area and height to width ratio, had to be quantitatively assessed. A calibration spheres dataset with more than 100 pieces for each nominal diameter value from 1.5 mm upward was analyzed, which revealed a slight tendency of the 50% mean smoothing algorithm to systematically decrease the area. As a countermeasure, the weights of inner and outer boundary had to be set to 48.2% and 51.8%, respectively. The result is shown in Fig. A4 with all parameter changes incurred by the smoothing algorithm being less than 1% on average.

## REFERENCES

Allnutt, J. E., 1989: *Satellite-to-Ground Radiowave Propagation.* Peter Peregrinus Ltd., on behalf of the Institute of Electrical Engineers, 421 pp.

Beard, K. V., and C. Chuang, 1987: A new model for the equilibrium shape of raindrops. *J. Atmos. Sci.,* **44,** 1509–1524.

——, and R. J. Kubesh, 1991: Laboratory measurements of small raindrop distortion. Part II: Oscillation frequencies and modes. *J. Atmos. Sci.,* **48,** 2245–2264.

Brandes, E. A., G. Zhang, and J. Vivekanandan, 2002: Experiments in rainfall estimation with a polarimetric radar in a subtropical environment. *J. Appl. Meteor.,* **41,** 674–684.

Bringi, V. N., and V. Chandrasekar, 2001: *Polarisation Doppler Weather Radar.* Cambridge University Press, 636 pp.

——, ——, J. Hubbert, E. Gorgucci, W. L. Randeu, and M. Schoenhuber, 2003: Raindrop size distribution in different climatic regimes from disdrometer and dual-polarized radar analysis. *J. Atmos. Sci.,* **60,** 354–365.

——, M. Thurai, K. Nakagawa, G. J. Huang, T. Kobayashi, A. Adachi, H. Hanado, and S. Sekizawa, 2006: Rainfall estimation from C-band polarimetric radar in Okinawa, Japan: Comparisons with 2D-video disdrometer and 400 MHz wind profiler, 2006. *J. Meteor. Soc. Japan,* **84,** 705–724.

Carey, L. D., S. A. Rutledge, D. A. Ahijevych, and T. D. Keenan, 2000: Correcting propagation effects in C-band polarimetric radar observations of tropical convection using differential propagation phase. *J. Appl. Meteor.,* **39,** 1405–1433.

Gimpl, J., 2003: Optimised algorithms for 2d-video-distrometer data analysis and interpretation. Diploma thesis, Institute of Communications and Wave Propagation, Graz University of Technology, Austria, 111 pp.

Goddard, J. W. F., K. L. Morgan, A. J. Illingworth, and H. Sauvageot, 1995: Dual wavelength polarization measurements in precipitation using the CAMRa and Rabelais radars. Preprints, *27th Int. Conf. Radar on Meteorology,* Vail, CO, Amer. Meteor. Soc., 196–198.

Keenan, T. D., L. D. Carey, D. S. Zrnic, and P. T. May, 2001:

Sensitivity of 5-cm wavelength polarimetric radar variables to raindrop axial ratio and drop size distribution. *J. Appl. Meteor.,* **40,** 526–545.

Kruger, A., and W. F. Krajewski, 2002: Two-dimensional video disdrometer: A description. *J. Atmos. Oceanic Technol.,* **19,** 602–617.

Meischner, P., V. N. Bringi, D. Heimann, and H. A. Hoeller, 1991: A squall line in southern Germany: Kinematics and precipitation formulation as deduced by advanced polarimetric and Doppler radar measurements. *Mon. Wea. Rev.,* **119,** 678–701.

Morgan, M. A., 1980: Finite element computation of microwave scattering by raindrops. *Radio Sci.,* **15,** 1109–1119.

Oguchi, T., 1977: Scattering properties of Pruppacher-and-Pitter form raindrops and cross polarization due to rain: Calculations at 11, 13, 19.3, and 34.8 GHz. *Radio Sci.,* **12,** 41–51.

——, 1983: Electromagnetic wave propagation and scattering in rain and other hydrometeors. *Proc. IEEE,* **71,** 1029–1079.

Olsen, R. L., 1981: Cross-polarization during precipitation on terrestrial links: A review. *Radio Sci.,* **16,** 781–812.

Pruppacher, H. R., and R. L. Pitter, 1971: A semi-empirical determination of the shape of cloud and rain drops. *J. Atmos. Sci.,* **28,** 86–94.

Randeu, W. L., M. Schönhuber, and G. Lammer, 2002: Real-time measurements and analyses of precipitation micro-structure and dynamics. *Proc. Second European Conf. on Radar Meteorology (ERAD),* Delft, Netherlands, Copernicus GmbH, 78–83.

Ray, P. S., 1972: Broadband complex refractive indices of ice and water. *Appl. Opt.,* **11,** 1836–1844.

Ryzhkov, A., and D. S. Zrnić, 1995: Precipitation and attenuation measurements at 10-cm wavelength. *J. Appl. Meteor.,* **34,** 2121–2134.

Schuur, T. J., A. V. Ryzhkov, D. S. Zrnic, and M. Schönhuber, 2001: Drop size distributions measured by a 2D video disdrometer: Comparison with dual-polarization radar data. *J. Appl. Meteor.,* **40,** 1019–1034.

Thurai, M., and V. N. Bringi, 2005: Drop axis ratios from 2D video disdrometer. *J. Atmos. Oceanic Technol.,* **22,** 963–975.

——, and H. Hanado, 2005: Absolute calibration of C-band weather radars using differential propagation phase in rain. *IEE Electron. Lett.,* **41,** 1405–1406.

——, G. J. Huang, V. N. Bringi, and M. Schönhuber, 2006: Drop shape probability contours in rain from 2-D video disdrometer: Implications for the "self-consistency method" at C-band. Extended abstracts, *Proc. Fourth European Conf. on Radar in Meteorology and Hydrology (ERAD),* Barcelona, Spain, Copernicus GmbH, P1.1.

Wang, P. K., 1982: Mathematical description of the shape of conical hydrometeors. *J. Atmos. Sci.,* **39,** 2615–2622.

——, T. J. Greenwald, and J. Wang, 1987: A three parameter representation of the shape and size distributions of hail stones—A case study. *J. Atmos. Sci.,* **44,** 1062–1070.